Research Article

Crystallization regulation of Fe⁰@Fe₃O₄ using a g-C₃N₄/diatomite composite for enhancing photocatalytic peroxymonosulfate activation

Xinlin Wang, Xiangwei Zhang, Haiqin Zhou, Chunquan Li, Zhiming Sun

School of Chemical and Environmental Engineering, China University of Mining and Technology (Beijing), Beijing 100083, China.

Correspondence to: Prof. Zhiming Sun, School of Chemical and Environmental Engineering, China University of Mining and Technology (Beijing), Beijing 100083, China. E-mail: zhimingsun@cumtb.edu.cn

Abstract

Photocatalysis and persulfate synergistic catalysis have recently become promising technologies for degrading refractory organic contaminants in effluents. In this work, $Fe^0@Fe_3O_4$ is successfully immobilized on a N-deficient g-C₃N₄/diatomite composite (NGD) via a simple self-assembly process. The structural characteristics and peroxymonosulfate activation ability of the composite under visible-light irradiation are explored in detail. Notably, the introduction of NGD affects the crystallinity and morphology of $Fe^0@Fe_3O_4$, forming homogenously distributed nanoparticles rather than irregular and agglomerated crystals with rod-like structures. The synthesized $Fe^0@Fe_3O_4$/N-deficient g-C₃N₄/diatomite composite (FNGD) exhibits a superior removal percentage of bisphenol A (> 95% within 15 min). Furthermore, its degradation rate constant (*k*) is ~59 and ~27 times higher than those of NGD and bare $Fe^0@Fe_3O_4$, respectively. Moreover, holes (h_{vb}^+), singlet oxygen ($^1O_2$) and superoxide free radicals ($^\cdot O_2^-$) play a major role in the FNGD/peroxymonosulfate/visible system based on radial quenching experiments and electron paramagnetic resonance spectra. Overall, this study provides novel insights into visible light-assisted peroxymonosulfate activation by the g-C₃N₄/mineral-based composite for wastewater treatment.

Keywords: Peroxymonosulfate, photocatalysis, iron oxide, diatomite, bisphenol A

INTRODUCTION

Water body pollution by xenobiotic chemicals has become a global issue that affects the survival of all living creatures[1,2]. In order to treat xenobiotic chemicals, various strategies, such as adsorption, precipitation, filtration and biological treatment, have been employed. In particular, advanced oxidation processes (AOPs) have become popular for removing contaminants from effluents in recent decades due to their excellent capability for high mineralizing rates[3-5]. Furthermore, photocatalysis has also emerged as a promising solution for the purification of effluents by solar energy harvesting. Graphitic carbon nitride (g-C_3N_4) is endowed with outstanding photocatalytic ability due to its narrow band gap (2.7 eV), non-toxicity and high stability. However, the low surface area and sluggish photogenerated carrier transfer of g-C_3N_4 hinder its wide application[6-8].

Therefore, the modification of g-C_3N_4 via doping or coupling with other materials (like Ag_3PO_4, BiOCl, $CoTiO_3$ and natural minerals) for improved surface area and better effluent cleaning performance has been reported[8]. Our group has already carried out work in adopting diatomite ($SiO_2 \cdot nH_2O$) as the carrier of g-C_3N_4 due to its physicochemical stability, the inhibiting effect for agglomeration and improved charge separation efficiency[9-11]. However, the low visible-light adsorption ability and high recombination rate of photogenerated electron-hole pairs are still limitations that restrict the large-scale application of materials in effluent treatment.

In addition, sulfate radical-advanced oxidation processes (SR-AOPs) have become important for the removal of recalcitrant pollutants, owing to their wider pH range (2-8) compared with Fenton systems (2-4)[12], high oxidation potential of 2.5-3.1 V *vs.* a standard hydrogen electrode and longer half-life ($t_{1/2}$ = 30-40 μs) compared with $^{\bullet}$OH ($t_{1/2} \leq 1$ μs). It has been indicated that $SO_4^{\bullet-}$ could be formed by radiation and thermal activation and carbon-based and metal catalysts[2,4]. Thereinto, iron-based catalysts, such as Fe^0, iron oxides and FeOOH, have been used as the most common activators of peroxymonosulfate (PMS) for water treatment due to their vast reserves, low cost, long-lasting activation and high performance[13-15]. Among these, $Fe^0@Fe_3O_4$ has been synthesized with the advantage of the stable production of Fe^{2+} from promoted electron transfer[16-18]. However, the agglomeration and secondary contamination caused by Fe leaching are unavoidable when using iron-containing catalysts.

To further overcome the limitations of g-C_3N_4/diatomite (GD) and iron-based catalysts, this study combines photocatalysis and SR-AOPs to synthesize $Fe^0@Fe_3O_4$/N-deficient g-C_3N_4/diatomite composites (FNGD). Notably, we systematically characterize the prepared FNGD materials, evaluate the catalytic performance of FNGD samples for PMS activation under visible-light irradiation and explore the involvement of active species including reactive oxygen species (ROS) together with photoexcited electron-hole pairs for the removal mechanism of bisphenol A (BPA). We also examine the effects of the operating parameters (BPA and PMS concentrations, pH value and catalyst dosage) and background species (inorganic anions) on the degradation performance of BPA in the 0.6-FNGD/PMS/Vis system.

EXPERIMENTAL

Materials

Dicyandiamide ($C_2H_4N_4$), ammonium persulfate [$(NH_4)_2S_2O_8$], ferrous acetate ($C_4H_6FeO_4 \cdot 4H_2O$), ethanol (C_2H_6O), L-histidine ($C_6H_9N_3O_2$), furfuryl alcohol (FFA, $C_5H_6O_2$), methanol (MeOH, CH_4O), tertiary butanol (TBA, $C_4H_{10}O$), 1,4-benzoquinone (BQ, $C_6H_4O_2$) and EDTA-2Na ($C_{10}H_{14}N_2Na_2O_8$) were purchased from Macklin Biochemical Co., Ltd (Shanghai, China). The diatomite utilized in this study was obtained from Linjiang City, Jilin Province, China, and was purified according to our previous report, which promoted its porosity and purity[19].

Sample preparation

g-C_3N_4 and GD were prepared according to our previous report[20]. N-deficient g-C_3N_4/diatomite (NGD) was synthesized through a thermal oxidation method. Typically, 5.0 g of diatomite (1.0 g) and dicyandiamide (4.0 g) were mixed uniformly with 1.5 g of $(NH_4)_2S_2O_8$ in an agate mortar. The product was then heated at 550 °C for 4 h under an air atmosphere with a heating rate of 2.3 °C/min.

The FNGD composites were synthesized as follows. Firstly, 0.5 g of NGD and x mmol of $C_4H_6FeO_4 \cdot 4H_2O$ (x = 0.2, 0.4, 0.6, 1.2 and 1.8) were dissolved into 5 mL of ethanol and then the suspension was sonicated for 2 h to be evenly dispersed. Subsequently, the suspension was transferred to a vacuum oven and dried at 70 °C. Finally, the powder was heated at 500 °C for 2 h under a nitrogen atmosphere with a heating rate of 5 °C/min. The samples prepared with x = 0.2, 0.4, 0.6, 1.2 and 1.8 are denoted as 0.2-FNGD, 0.4-FNGD, 0.6-FNGD, 1.2-FNGD and 1.8-FNGD, respectively. Furthermore, pure samples of $Fe^0@Fe_3O_4$ were synthesized using the above methods without the introduction of NGD.

Characterization

X-ray powder diffraction (XRD) was applied to investigate the phase structure of the prepared materials. Fourier transformed infrared (FTIR) spectroscopy was performed to analyze the interaction of prepared materials. Scanning electron microscopy (SEM) and energy-dispersive spectroscopy (EDS) were employed to observe the morphologies and elemental distribution of the prepared FNGD materials, respectively. The pore structure parameters of the as-prepared samples were obtained using multipoint N_2 adsorption/desorption isotherms with Brunauer-Emmett-Teller (BET) and Barrett-Joyner-Halenda (BJH) methods. X-ray photoelectron spectroscopy (XPS) was applied to identify the surface chemical bonds of the 0.6-FNGD composite. Ultraviolet-visible diffuse reflectance spectroscopy (UV-vis DRS) was applied to observe the optical adsorption and band structure of the FNGD and contrastive samples. The electrochemical properties, including the electrochemical impedance spectroscopy and transient photocurrent response, of selected samples were tested. Inductively coupled plasma optical emission spectrometry (ICP-OES) was used to detect the Fe leaching concentration and Fe ion content of 0.6-FNGD. Electron paramagnetic resonance (EPR) was applied under different reaction systems.

Evaluation of catalytic activity

In the degradation process, 15 mg of x-FNGD were dispersed into 30 mL of BPA solution (15 mg/L). Afterward, the suspension was dispersed uniformly under ultrasound for 1 min and then stirred in dark conditions for 15 min to achieve the adsorption-desorption equilibrium. Subsequently, a PMS solution (0.30 mL, 30 mmol/L) was added to the above suspension and a xenon lamp (300 W, > 420 nm) with an irradiance of $35.92 \times 10^{-2} W/cm^2$ was immediately turned on[21]. At expected time intervals, 1 mL of suspension was sampled and mixed with 0.5 mL of methanol to end the reaction. The mixed liquid was then filtrated by a 0.22 μm filter.

The concentration of BPA was evaluated using high-performance liquid chromatography (LC-2030C Shimadzu, Japan) with a C18 reverse-phase column. The mobile phase consisted of ultrapure water (40%) and acetonitrile (60%) with a flow rate of 1.0 mL/min. The detection wavelength was 223 nm and the injection volume was 10 μL.

RESULTS AND DISCUSSION

Characterization of catalysts

The phase structures of the $Fe^0@Fe_3O_4$, NGD and FNGD composites are exhibited in Figure 1A. The XRD pattern of pure $Fe^0@Fe_3O_4$ shows the characteristic peaks at $2\theta = 35.42°$ and $44.68°$, which correspond to the lattice planes of magnetite (JCPDS No. 19-0629)[22] and iron (JCPDS No. 87-0721)[23], respectively,
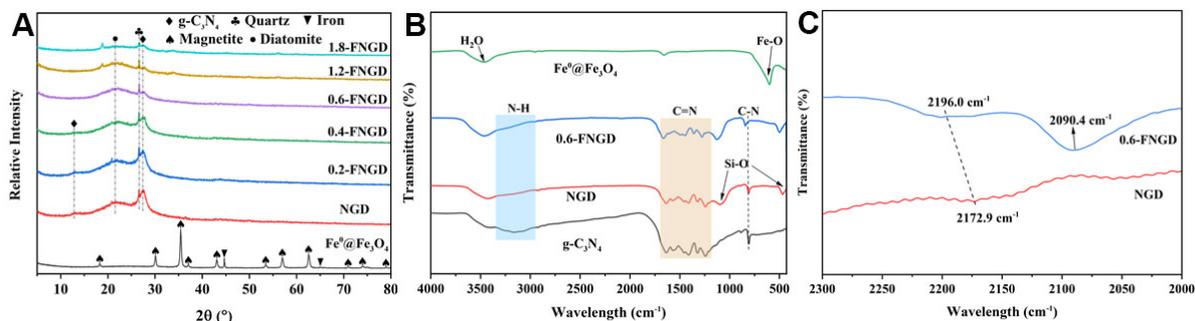
Figure 1. (A) XRD patterns of $Fe^0@Fe_3O_4$, NGD and the prepared FNGD composites. (B) FTIR spectra of 0.6-FNGD composite and contrastive samples. (C) Partial enlargements of FTIR spectra.

suggesting the successful synthesis of $Fe^0@Fe_3O_4$. However, the prepared FNGD composites did not exhibit any characteristic peaks of magnetite and iron. The possible reason for this phenomenon is explained in the XPS part. Furthermore, the peaks centered at $2\theta = 21.8°$ and 26.70° in the XRD patterns of the NGD and FNGD composites are attributed to amorphous SiO_2[24] and quartz impurities[25], respectively. Furthermore, the XRD patterns of NGD, 0.2-FNGD and 0.4-FNGD all show characteristic peaks at 12.85° and 27.55°, corresponding to the lattice planes of $g-C_3N_4$ (JCPDS No. 87-1526)[10], suggesting the good assembly of $g-C_3N_4$ on the diatomite surface. However, the patterns of 0.6-FNGD, 1.2-FNGD and 1.8-FNGD did not exhibit the characteristic peak at 12.85°, which might be due to the introduction of excessive Fe affecting the crystallinity of $g-C_3N_4$.

Furthermore, the chemical structures of $g-C_3N_4$, NGD, 0.6-FNGD and $Fe^0@Fe_3O_4$ were analyzed by FTIR, as shown in Figure 1B. For the prepared $g-C_3N_4$, the two broad adsorption peaks at 3450 and 3350-2950 cm^{-1} were caused by the O-H (adsorbed H_2O) and N-H stretching vibrations. The N-H bond results from the incomplete polycondensation of the edges of the s-triazine ring system. The adsorption peaks at 1200-1650 and 809 cm^{-1} originate from the typical stretching vibration of C=N and C-N heterocycles[26]. For the NGD material, two fresh adsorption peaks centered at 1100 and 468 cm^{-1} appeared, belonging to the Si-O stretching vibration of diatomite[27]. The adsorption peak at ~3658-3345 cm^{-1} is attributed to the stretching vibration of the Si-OH groups[28]. The above results indicate that the chemical structure of diatomite and $g-C_3N_4$ is well preserved in NGD. For the 0.6-FNGD material, the structural features of $g-C_3N_4$ and diatomite are also preserved after the preparation process. Furthermore, two new peaks at 2000-2300 cm^{-1} belonging to C≡N stretching appeared in the spectra of 0.6-FNGD [Figure 1C], which is likely due to the introduction of N vacancies[29]. Overall, the absorption peaks of NGD, 0.6-FNGD and $Fe^0@Fe_3O_4$ in the FTIR spectra are consistent with the XRD results, further suggesting the successful synthesis of FNGD materials.

The morphologies of the diatomite, $Fe^0@Fe_3O_4$ and 0.6-FNGD are shown in Figure 2. The diatomite [Figure 2A] exhibited a smooth and disk-like morphology with well-distributed macropores of ~500 nm, which is beneficial for loading catalysts. $Fe^0@Fe_3O_4$ [Figure 2B] was endowed with an irregular rod-like structure and aggregated by particles with a diameter of ~15-50 nm, which is adverse for contact with PMS and organic pollutants. As for the prepared 0.6-FNGD composite, the surface of the diatomite became rougher and the SEM-EDS elemental mappings indicate that the elements of C, N and Fe were homogeneously dispersed on the surface of the diatomite. This suggests the successful combination of $g-C_3N_4$ and $Fe^0@Fe_3O_4$ on the diatomite surface[10]. This combination would afford more active sites and further promote the generation of reactive species with enhanced separation and transfer efficiency of photoexcited electron-hole pairs for outstanding catalytic efficiency. Overall, the results of EDS, FTIR and
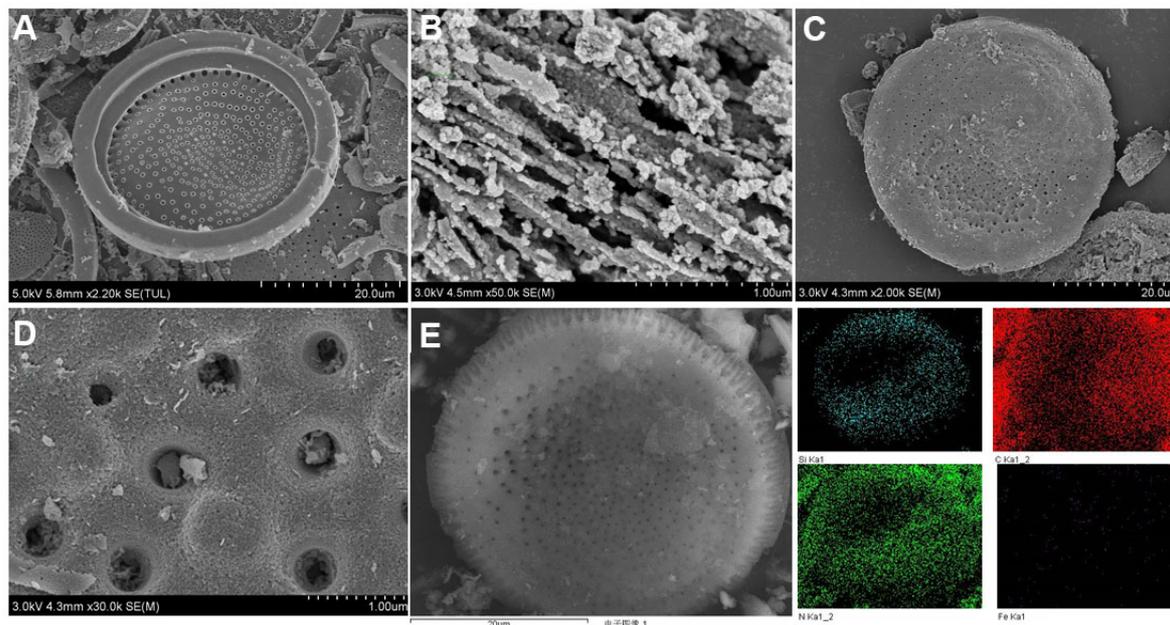
Figure 2. SEM images of (A) diatomite, (B) $Fe^0@Fe_3O_4$, (C and D) 0.6-FNGD and (E) SEM-EDS elemental mapping of Si, C, N and Fe for 0.6-FNGD composite.

XRD all demonstrate the successful synthesis of the ternary FNGD composite.

For the further investigation of the pore structural parameters of the diatomite, $g\text{-}C_3N_4$, $Fe^0@Fe_3O_4$, NGD and 0.6-FNGD composites, the obtained N_2 adsorption/desorption isotherms and pore diameter distribution curves are exhibited in Figure 3. The results of the BET surface area, pore volume and average pore diameter are also calculated and listed in Table 1. As illustrated in Figure 3A, diatomite exhibited a typical II adsorption isotherm representative of the presence of a nonporous or macroporous structure. In contrast, $g\text{-}C_3N_4$, $Fe^0@Fe_3O_4$, NGD and 0.6-FNGD all presented typical IV adsorption isotherms with an H3 hysteresis loop, suggesting the presence of a mesoporous structure[10,30]. In addition, the pore size distribution was concentrated with the tendency of small pore sizes for 0.6-FNGD, as exhibited in Figure 3B, which might be due to the uniform loading of $Fe^0@Fe_3O_4$ substances onto the NGD.

As listed in Table 1, compared with diatomite, $g\text{-}C_3N_4$, $Fe^0@Fe_3O_4$ and NGD, 0.6-FNGD has a larger specific surface area (38.61 m²/g) and higher pore volume (0.177 cm³/g). This suggests that the ternary FNGD catalyst might have a good adsorption performance and more contact opportunities for active sites with PMS and BPA, thus improving the catalytic degradation performance.

The chemical composition and binding bonds of 0.6-FNGD were further investigated by XPS, as displayed in Figure 4. The survey scan of 0.6-FNGD exhibited the characteristic peaks of Si 2p, C 1s, N 1s, O 1s and Fe 2p. In the Si 2p spectra of 0.6-FNGD, the peak at 104.2 eV can be ascribed to the Si-O-C bond, owing to the bonding between the surface oxygen atom of diatomite and the carbon atom of $g\text{-}C_3N_4$. As exhibited in Figure 4C, the O 1s curve of 0.6-FNGD showed three peaks at 533.1, 532.3 and 531.8 eV, which were attributed to the Si-O bond of SiO_2, the surface OH of diatomite and N-C-O bonds, respectively[31,32]. This result indicates the successful bonding between $g\text{-}C_3N_4$ and the microsized diatomite particles.

Table 1. BET surface area, pore volume and average pore size of diatomite, g-C$_3$N$_4$, Fe^0@Fe$_3$O$_4$, NGD and 0.6-FNGD composites

Sample	S_{BET} (m^2/g)	Total pore volume (cm^3/g)	Average pore diameter (nm)
Diatomite	15.45	0.046	11.8
g-C$_3$N$_4$	18.71	0.102	21.7
Fe^0@Fe$_3$O$_4$	28.71	0.106	14.8
NGD	25.29	0.132	20.8
0.6-FNGD	38.61	0.177	18.3
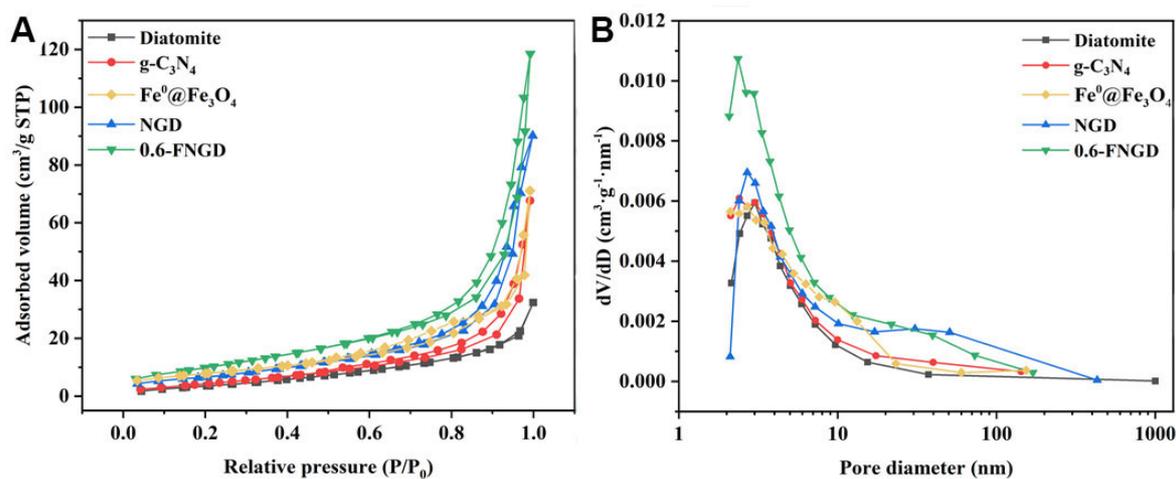
Figure 3. (A) N$_2$ adsorption-desorption isotherms and (B) BJH pore size distribution plots of diatomite, g-C$_3$N$_4$, Fe^0@Fe$_3$O$_4$, NGD and 0.6-FNGD.
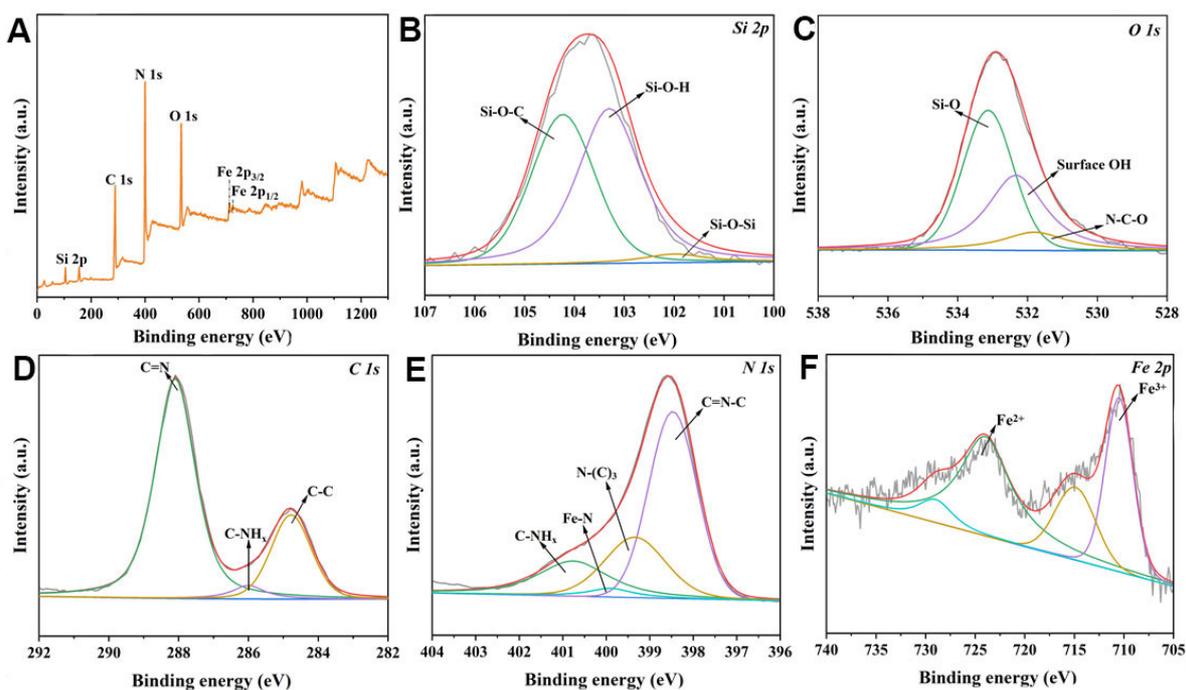
Figure 4. (A) Full XPS spectra and survey spectra of (B) Si 2p, (C) O 1s, (D) C 1s, (E) N 1s and (F) Fe 2p for 0.6-FNGD material.

In addition, three peaks at 288.1, 286.0 and 284.78 eV in the C 1s spectrum were caused by the C=N, C-NH$_x$ and C-C bonds of g-C$_3$N$_4$ and NGD, respectively[33]. However, the binding energy of hybridized N (C=N-C) shifted to 398.47 eV and the Fe-N located at 399.9 eV proves that the Fe species were stabilized in the electron-rich g-C$_3$N$_4$[34], which was in good agreement with the result of Fe ions leaching in the 0.6-FNGD material. More importantly, the chemical bonding between Fe and N [Figure 4E], which are the active sites[23] that might affect the crystal phase of magnetite and iron metal in the catalytic reaction, with implementation of crystallization regulation of Fe^0@Fe$_3$O$_4$. As shown in Figure 4F, the two peaks at 710.5 and 724.0 eV were ascribed to Fe^{3+} and Fe^{2+}, respectively. Nevertheless, the peak of Fe^0 at ~706 eV is not observed, which might be attributed to the limited XPS detection depth (< 10 nm) and the fact that the catalyst can be oxidized by air[35].

To assess the effect of the amount of Fe^0@Fe$_3$O$_4$ on the optical adsorption and band structure of FNGD, the UV-vis diffuse reflectance spectra of 0.6-FNGD, 0.4-FNGD, 0.2-FNGD and NGD were investigated. As shown in Figure 5A, FNGD not only exhibited inherent optical adsorption of g-C$_3$N$_4$ with an adsorption edge at 460 nm that originates from the π-conjugated C-N heterocycles, but also showed a gradually stronger uplift of the absorption tail in the range of 450-800 nm. Furthermore, the direct bandgap (E$_g$) results of FNGD [Figure 5B] indicate that the value of E$_g$ decreases gradually somewhat with the introduction of Fe^0@Fe$_3$O$_4$, suggesting its promotional effect on the visible-light adsorption ability of NGD.

As depicted in Figure 6A, a much smaller arc radius of the Nyquist circle was observed in the presence of 0.6-FNGD than that of GD, reflecting a lower internal electron transfer resistance. This proves that 0.6-FNGD features greatly improved charge separation and transfer efficiency of generated electron-hole pairs[36]. In addition, some selected materials, including 0.6-FNGD, NGD and NG, showed obvious photocurrent responses during the repeated light (on/off) cycles, as shown in Figure 6B[37]. The photocurrent response order was 0.6-FNGD (1.72 × 10^{-6}) > NGD (1.57 × 10^{-6}) > NG (1.43 × 10^{-6}). This result suggests that the combination of NG with diatomite and the introduction of Fe^0@Fe$_3$O$_4$ effectively improved the separation and transfer efficiency of electron-hole pairs[38].

Catalytic efficiency of catalysts

The catalytic efficiency of the NGD, Fe^0@Fe$_3$O$_4$ and FNGD composites was evaluated for BPA degradation by activating PMS under visible-light irradiation [Figure 7A]. The removal percentage of BPA was only 11% for NGD and 17% for Fe^0@Fe$_3$O$_4$ after 15 min, indicating their poor catalytic activity. In contrast, the FNGD composites presented a high removal percentage (> 87%) of BPA within 15 min, showing that the combination of Fe^0@Fe$_3$O$_4$ and NGD contributes to the successful construction of efficient catalytic materials. The removal percentage of BPA for 0.6-FNGD and 1.2-FNGD was similar (> 95% within 15 min). Hereupon, the prepared 0.6-FNGD (Fe ion content = 5.56 wt.% by ICP-OES) was chosen as the optimum material for all the following experiments. However, the degradation velocity of BPA decreased when further increasing the amount of C$_4$H$_6$FeO$_4$·4H$_2$O from 1.2 to 1.8 mmol. The reason is that the corresponding coverage of Fe^0@Fe$_3$O$_4$ on the NGD might be incomplete, thus weakening the interactions between Fe^0@Fe$_3$O$_4$ and NGD[39].

The pseudo-first-order kinetic constant (*k*) in linear transforms Ln(C_0/C_t) = *kt* of BPA degradation on NGD, Fe^0@Fe$_3$O$_4$ and some selected FNGD composites are displayed in Figure 7B. Among these, 0.6-FNGD exhibited a high reaction activity (*k* = 322 × 10^{-5} s^{-1}) that was 59 times higher than NGD (*k* = 5.43 × 10^{-5} s^{-1}) and 27 times higher than Fe^0@Fe$_3$O$_4$ (*k* = 11.89 × 10^{-5} s^{-1}), illustrating the superior degradation rate of BPA in the FNGD/PMS/Vis system and proving the superiority of the FNGD composites. Furthermore, as exhibited in Figure 7C, only 2% and 1% of BPA were removed in the PMS alone and Vis alone systems,
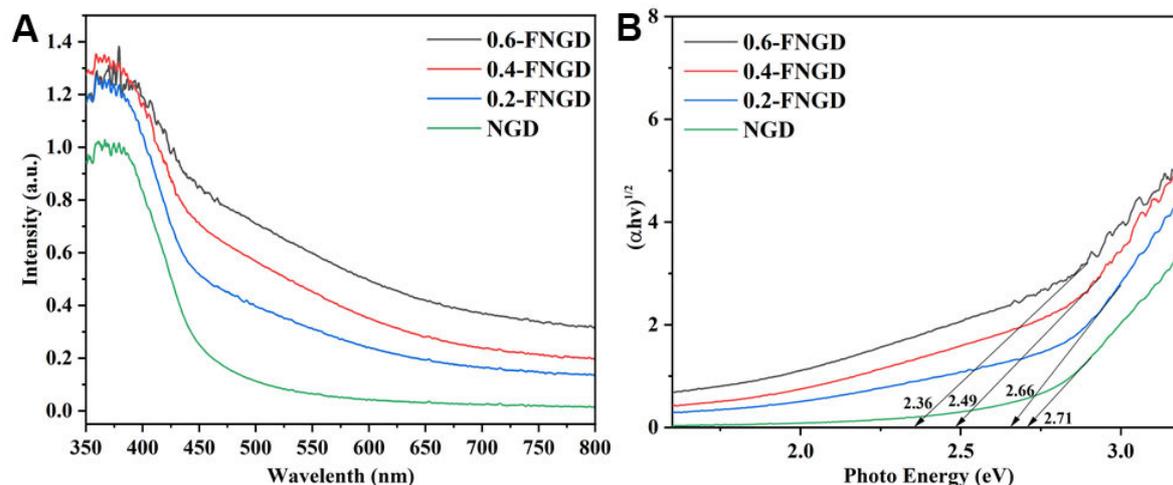
Figure 5. (A) UV-vis DRS and (B) band gaps of NGD and selected FNGD materials.
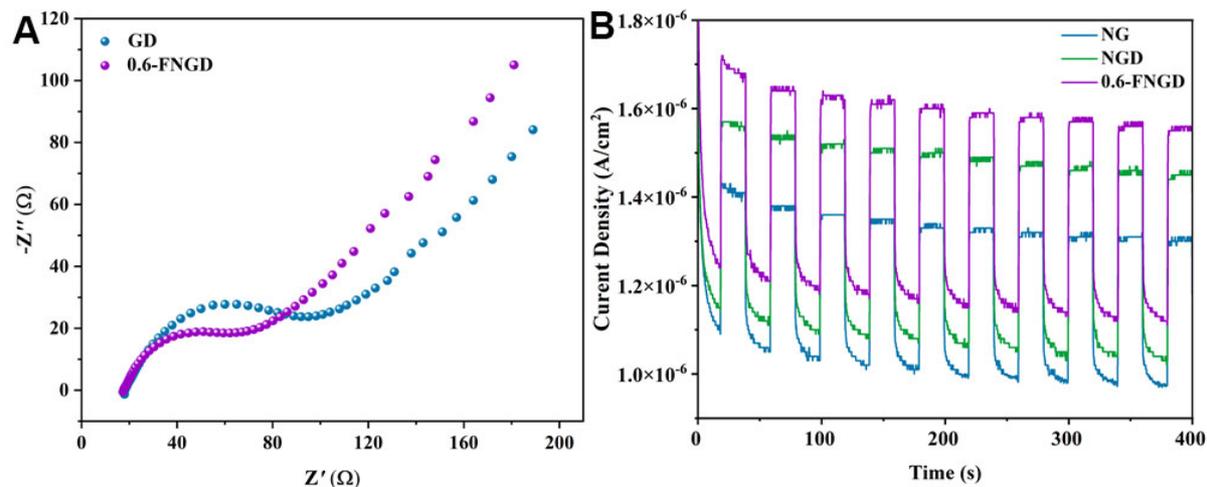
Figure 6. (A) Electrochemical impedance spectroscopy and (B) transient photocurrent response of 0.6-FNGD and contrastive samples.

respectively, suggesting that PMS or visible light cannot degrade BPA directly. Notably, the removal percentage of BPA reached up to 98% in the 0.6-FNGD/PMS/Vis system, suggesting the synergistic effect between PMS and visible-light irradiation[40].

To determine the practical application of the 0.6-FNGD/PMS/Vis system, the effects of BPA and PMS concentrations and catalyst dosages on BPA degradation were explored [Figure 7D-F]. As shown in Figure 7D, BPA can be removed completely within 5 and 10 min at the initial concentrations of 5 and 15 mg/L, respectively, suggesting the prepared 0.6-FNGD composite is an efficient catalyst in the PMS/Vis system. Nevertheless, when the initial BPA concentrations were 25 and 35 mg/L, only 72% and 57% removal percentages can be obtained after 15 min. This phenomenon can be attributed to the mutual competition of BPA for ROS, electron-hole pairs[39] and a higher organic load under the same amount of oxidants. Furthermore, when the reaction time was prolonged to 60 min, 89% and 72% removal percentages were obtained for the BPA concentrations of 25 and 35 mg/L, respectively.
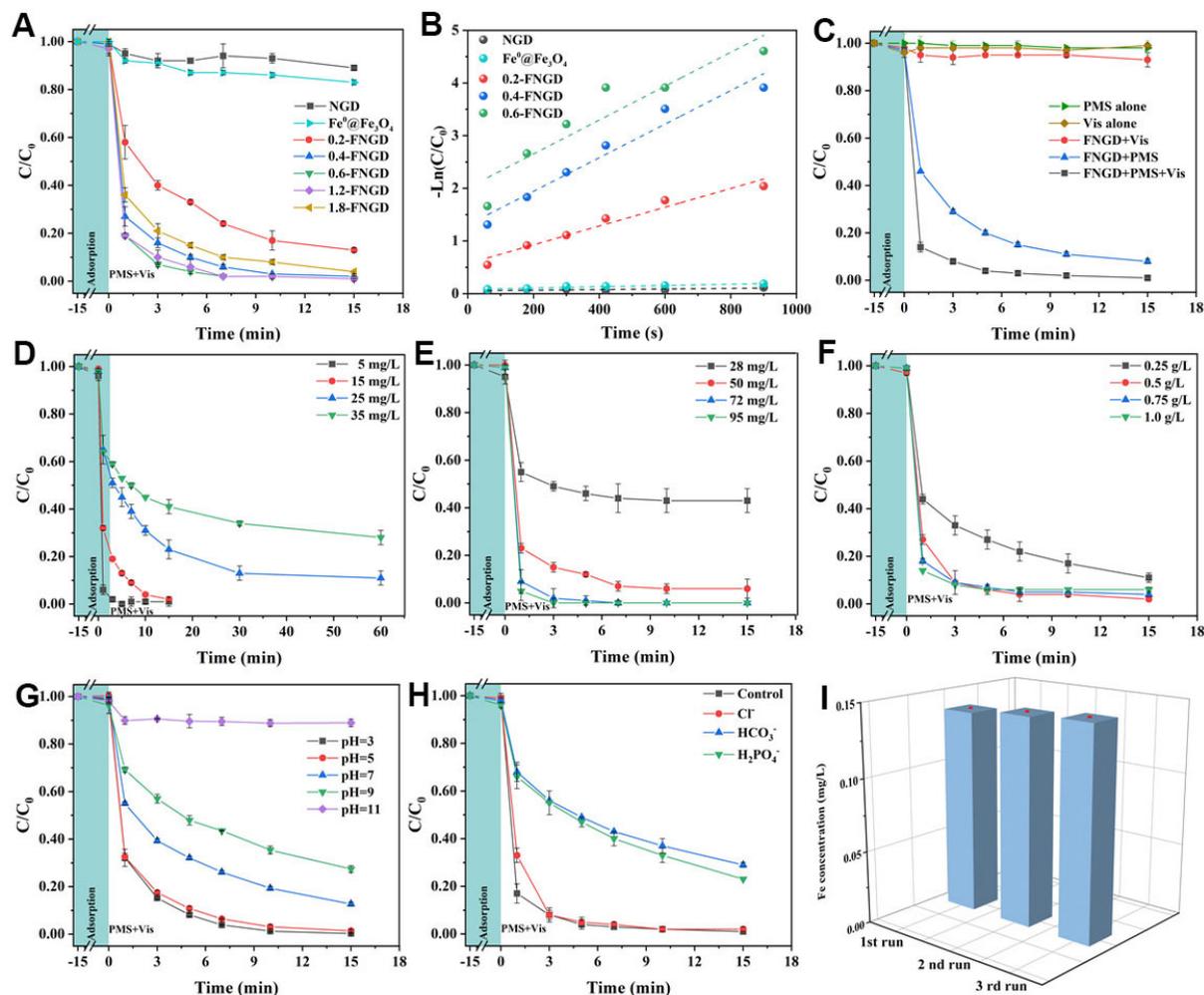
Figure 7. Removal of (A) BPA and (B) linear transform $\ln(C_0/C)$ of kinetic curves of NGD, $Fe^0@Fe_3O_4$ and the prepared FNGD composites. (C) Removal of BPA in different systems. Effect of (D) BPA concentration, (E) PMS concentration, (F) 0.6-FNGD dosage, (G) initial pH and (H) inorganic anion effect on BPA degradation in 0.6-FNGD/PMS/Vis system. (I) Fe leaching concentration of 0.6-FNGD during the degradation process. General conditions: C_0 (BPA) = 15 mg/L, C_0 (catalyst) = 0.5 g/L, C_0 (PMS) = 50 mg/L, V = 30 mL, temperature = 293 K, initial pH = 7.0.

As exhibited in Figure 7E, the degradation of BPA was rapidly promoted with the increase of PMS dosage from 28 to 72 mg/L. In contrast, the increasing velocity decreased with excessive PMS dosage, especially from 72 to 95 mg/L, which might be attributed to the excessive PMS promoting competitive reactions that consume oxidants and the limited generation rate of active species without extra 0.6-FNGD[41]. As exhibited in Figure 7F, the removal percentage of BPA was rapidly promoted when the 0.6-FNGD dosage increased from 0.25 to 0.5 g/L, suggesting that the extra 0.6-FNGD dosage could provide more available active sites when the amount of catalyst is relatively low.

In addition, the effects of pH (3-11) and inorganic anions (Cl$^-$, HCO$_3^-$, H$_2$PO$_4^-$) on BPA degradation were also explored [Figure 7G and H]. As displayed in Figure 7G, the removal percentages of BPA were maintained well in the pH range from 3 to 9 (> 73% within 15 min) and decreased rapidly when the pH value was 11. The sudden drop at pH = 11 was due to the generation of SO_5^{2-}, which prevented the generation of $SO_4^{\bullet-}$ and $^{\bullet}OH$ in the 0.6-FNGD/PMS/Vis system[42]. Thus, the prepared FNGD material can be

applied well in weakly acidic or alkaline environments. As shown in Figure 7H, no obvious effect on BPA degradation could be noticed after the addition of Cl^{-}. As for HCO_3^- and $H_2PO_4^-$, the inhibition effect was observed, mainly owing to the strong quenching of HCO_3^- for $SO_4^{\bullet-}$ and $^{\bullet}OH$[43], as well as the complexation of $H_2PO_4^-$ with iron[44]. Furthermore, the addition of HCO_3^- and $H_2PO_4^-$ can also increase the pH value and induce a decrease in the removal percentage of BPA[45].

In addition, the Fe leaching concentration of 0.6-FNGD in the BPA degradation process was studied by ICP-OES analysis. As displayed in Figure 7I, the Fe leaching concentration of 0.6-FNGD after three cycles is lower than 0.15 mg/L, which is below the Chinese Surface Water Environmental Quality Standard (Fe is 0.30 mg/L stipulated in GB 3838-2002). Overall, the above results indicate that the 0.6-FNGD/PMS/Vis system is efficient and environmentally friendly for BPA removal.

Reaction mechanism

To identify the involved reactive species in the FNGD/PMS/Vis system, a quenching experiment was conducted using TBA (20 mM), MeOH (20 mM), BQ (10 mM), L-histidine (50 mM), FFA (50 mM) and EDTA-2Na (10 mM) to capture $^{\bullet}OH$, $SO_4^{\bullet-}$, $^{\bullet}O_2^-$, $^1O_2$ and h_{vb}^+, respectively. As displayed in Figure 8A, the removal percentage of BPA decreased slightly when adding TBA and MeOH, suggesting that $^{\bullet}OH$ and $SO_4^{\bullet-}$ acted in a secondary role in the FNGD/PMS/Vis system. Impressively, when BQ, L-histidine, FFA and EDTA-2Na were added, the removal percentage of BPA decreased to 44%, 13%, 11% and 9%, respectively, indicating that the $^{\bullet}O_2^-$, $^1O_2$ and h_{vb}^+ play a major role in the degradation process with the significant order of $h_{vb}^+ > {}^1O_2 > {}^{\bullet}O_2^-$. Overall, radical and non-radical pathways work together to oxidize pollutants in the FNGD/PMS/Vis system.

In-situ EPR was further applied to detect the generated reactive species in the PMS and PMS+Vis systems. As displayed in Figure 8B-D, the characteristic signals for $^1O_2$ (totality 3), $^{\bullet}O_2^-$ (totality 4), $^{\bullet}OH$ (totality 4) and $SO_4^{\bullet-}$ (totality 6) were obtained in the FNGD/PMS and FNGD/PMS/Vis systems. Furthermore, the signal intensity of $^1O_2$ in the FNGD/PMS/Vis system was stronger than that in the FNGD/PMS system, proving the synergetic effect of PMS under visible-light irradiation. Likewise, the signal enhancement was also observed in Figure 8C and D, which was consistent with the results of the above characterization and degradation experiments.

Based on the above results, the possible mechanism of BPA removal in the FNGD/PMS/Vis system is proposed and displayed below: (1) g-C_3N_4 and $Fe^0@Fe_3O_4$ generate electron-hole pairs [Equations 1 and 2] under visible-light irradiation with improved optical adsorption ability, transfer efficiency and charge separation by heterojunction, thereby enhancing the photocatalytic performance[46]; (2) the $^{\bullet}O_2^-$ reacts with h_{vb}^+ and H^+ to generate $^1O_2$ [Equations 3 and 4]; (3) the generated e_{cb}^- (from g-C_3N_4 and $Fe^0@Fe_3O_4$) and Fe^{2+} (from Fe^0 and Fe_3O_4) can also react with PMS to produce ROS [Equations 5-11][16]; (4) the prepared FNGD is beneficial to expose more active sites through increased BET and pore volume. Furthermore, the surface -OH of diatomite can facilitate the activation of PMS to generate $SO_4^{\bullet-}$ and $^{\bullet}OH$[45]. The possible generation methods of radicals and non-radicals following the significant order ($h_{vb}^+ > {}^1O_2 > {}^{\bullet}O_2^- > {}^{\bullet}OH$ and $SO_4^{\bullet-}$) in the FNGD/PMS/Vis system are listed below:

$$g - C_3N_4 + h\nu \rightarrow g - C_3N_4(e_{cb}^- + h_{vb}^+) \tag{1}$$

$$Fe^0 @Fe_3O_4 + h\nu \rightarrow Fe^0 @Fe_3O_4(e_{cb}^- + h_{vb}^+) \tag{2}$$

$$h_{vb}^+ + {}^\bullet O_2^- \rightarrow {}^1 O_2 \tag{3}$$

$$2{}^\bullet O_2^- + 2H^+ \rightarrow H_2O_2 + {}^1 O_2 \tag{4}$$

$$HSO_5^- + SO_5^{2-} \rightarrow SO_4^{2-} + HSO_4^- + {}^1 O_2 \tag{5}$$

$$e_{cb}^- + O_2 \rightarrow {}^\bullet O_2^- \tag{6}$$

$$h_{vb}^+ + H_2O \rightarrow {}^\bullet OH + H^+ \tag{7}$$

$$e_{cb}^- + HSO_5^- \rightarrow {}^\bullet OH + SO_4^{2-} \tag{8}$$

$$e_{cb}^- + HSO_5^- \rightarrow OH^- + SO_4^{\bullet -} \tag{9}$$

$$Fe^{2+} + HSO_5^- \rightarrow Fe^{3+} + SO_4^{\bullet -} + OH^- \tag{10}$$

$$Fe^{2+} + HSO_5^- \rightarrow Fe^{3+} + SO_4^{2-} + {}^\bullet OH \tag{11}$$
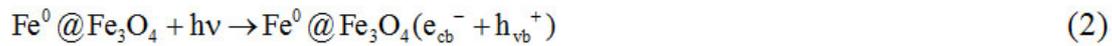
CONCLUSION

$Fe^0@Fe_3O_4$/N-deficient g-C_3N_4/diatomite composites were successfully synthesized. The prepared 0.6-FNGD material exhibited an excellent reaction rate constant (k = 322 × 10^{-5} s^{-1}), which was up to ~59 and ~27 times higher than that of N-deficient g-C_3N_4/diatomite (k = 5.43 × 10^{-5} s^{-1}) and bare $Fe^0@Fe_3O_4$ (k =11.89 × 10^{-5} s^{-1}) under the PMS/Vis system. The introduction of NGD affects the crystallization and morphology of $Fe^0@Fe_3O_4$. Furthermore, the composite exhibited higher specific surface area and pore volume, stronger visible light adsorption ability, improved separation and transfer efficiency of electron-hole pairs, low Fe leaching concentration after three cycles and boosted valance state cycling of iron, resulting in environmental-friendly and superior BPA degradation performance (> 95%; 15 min) under PMS/Vis system. The results of EPR and free radical quenching experiment show that radicals and non-radicals work together for catalytic oxidation and the significant order was h_{vb}^+ > ${}^1O_2$ > ${}^\bullet O_2^-$ > ${}^\bullet OH$ and $SO_4^{\bullet -}$ in the FNGD/PMS/Vis system. This study provides innovative strategies for the rational design of g-C_3N_4/natural mineral-based catalytic materials for PMS activation under visible-light irradiation for wastewater remediation.
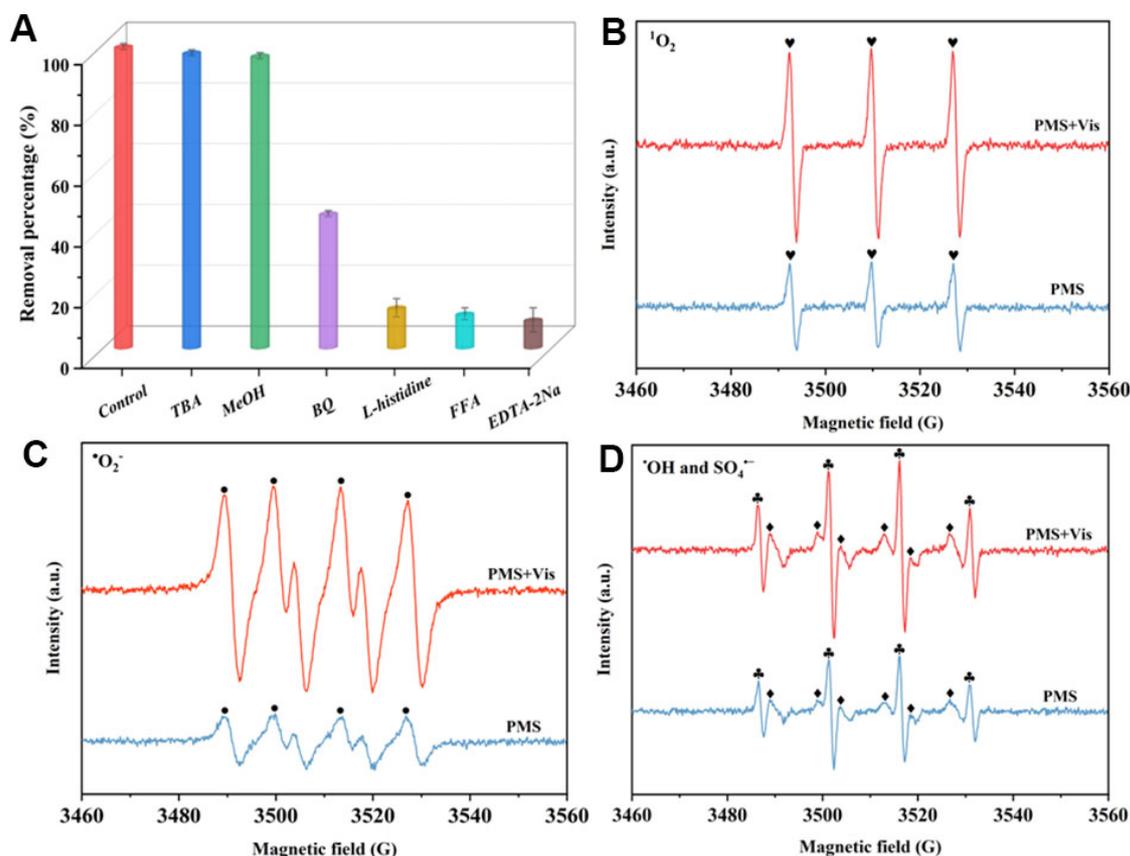
Figure 8. (A) Effects of different scavengers on BPA removal. EPR spectra of (B) $^1O_2$, (C) $^{\bullet}O_2^-$, (D) $^{\bullet}OH$ and $SO_4^{\bullet-}$ over 0.6-FNGD in different systems.

DECLARATIONS

Authors' contributions
Conceptualization, investigation, writing - original draft: Wang X
Methodology, investigation: Zhang X, Zhou H
Supervision, writing - review & editing: Li C
Conceptualization, writing - review & editing, funding acquisition, resources: Sun Z

Availability of data and materials
Not applicable.

Financial support and sponsorship

Conflicts of interest
None.

Ethical approval and consent to participate
Not applicable.

Copyright

© The Author(s) 2022.

REFERENCES

1. Crini G, Lichtfouse E. Advantages and disadvantages of techniques used for wastewater treatment. *Environ Chem Lett* 2019;17:145-55. DOI

2. Yaqoob AA, Parveen T, Umar K, Mohamad Ibrahim MN. Role of nanomaterials in the treatment of wastewater: a review. *Water* 2020;12:495. DOI

3. Dharupaneedi SP, Nataraj SK, Nadagouda M, Reddy KR, Shukla SS, Aminabhavi TM. Membrane-based separation of potential emerging pollutants. *Sep Purif Technol* 2019;210:850-66. DOI PubMed PMC

4. Ganzenko O, Huguenot D, van Hullebusch ED, Esposito G, Oturan MA. Electrochemical advanced oxidation and biological processes for wastewater treatment: a review of the combined approaches. *Environ Sci Pollut Res Int* 2014;21:8493-524. DOI PubMed

5. Oh W, Dong Z, Lim T. Generation of sulfate radical through heterogeneous catalysis for organic contaminants removal: Current development, challenges and prospects. *Applied Catalysis B: Environmental* 2016;194:169-201. DOI

6. Chen X, Shi R, Chen Q, et al. Three-dimensional porous g-C_3N_4 for highly efficient photocatalytic overall water splitting. *Nano Energy* 2019;59:644-50. DOI

7. Oliveros AN, Pimentel JAI, de Luna MDG, Garcia-segura S, Abarca RRM, Doong R. Visible-light photocatalytic diclofenac removal by tunable vanadium pentoxide/boron-doped graphitic carbon nitride composite. *Chem Engin J* 2021;403:126213. DOI

8. Paragas LKB, Dien Dang V, Sahu RS, et al. Enhanced visible-light-driven photocatalytic degradation of acetaminophen over CeO_2/I, K-codoped C_3N_4 heterojunction with tunable properties in simulated water matrix. *Sep Purif Technol* 2021;272:117567. DOI

9. Zhang X, Li C, Chen T, et al. Enhanced visible-light-assisted peroxymonosulfate activation over MnFe2O4 modified g-C3N4/diatomite composite for bisphenol A degradation. *Int J Min Sci Techn* 2021;31:1169-79. DOI

10. Yuan F, Sun Z, Li C, Tan Y, Zhang X, Zheng S. Multi-component design and in-situ synthesis of visible-light-driven SnO_2/g-C_3N_4/diatomite composite for high-efficient photoreduction of Cr(VI) with the aid of citric acid. *J Hazard Mater* 2020;396:122694. DOI PubMed

11. Jiang Z, Zhu H, Guo W, et al. Ag_3VO_4/g-C_3N_4/diatomite ternary compound reduces Cr(vi) ion in aqueous solution effectively under visible light. *RSC Adv* 2022;12:7671-9. DOI PubMed PMC

12. Xiao S, Cheng M, Zhong H, et al. Iron-mediated activation of persulfate and peroxymonosulfate in both homogeneous and heterogeneous ways: a review. *Chem Engin J* 2020;384:123265. DOI

13. Cao J, Lai L, Lai B, Yao G, Chen X, Song L. Degradation of tetracycline by peroxymonosulfate activated with zero-valent iron: performance, intermediates, toxicity and mechanism. *Chem Engin J* 2019;364:45-56. DOI

14. Fan J, Zhao Z, Ding Z, Liu J. Synthesis of different crystallographic FeOOH catalysts for peroxymonosulfate activation towards organic matter degradation. *RSC Adv* 2018;8:7269-79. DOI PubMed PMC

15. Long Y, Li S, Su Y, et al. Sulfur-containing iron nanocomposites confined in S/N co-doped carbon for catalytic peroxymonosulfate oxidation of organic pollutants: Low iron leaching, degradation mechanism and intermediates. *Chem Engin J* 2021;404:126499. DOI

16. Wang S, Wang J. Synergistic effect of PMS activation by Fe^0@Fe_3O_4 anchored on N, S, O co-doped carbon composite for degradation of sulfamethoxazole. *Chem Engin J* 2022;427:131960. DOI

17. Yan Y, Zhang H, Wang W, Li W, Ren Y, Li X. Synthesis of Fe^0/Fe_3O_4@porous carbon through a facile heat treatment of iron-containing candle soots for peroxymonosulfate activation and efficient degradation of sulfamethoxazole. *J Hazard Mater* 2021;411:124952. DOI PubMed

18. Wan D, Li W, Wang G, Lu L, Wei X. Degradation of p-Nitrophenol using magnetic Fe^0/Fe_3O_4/Coke composite as a heterogeneous Fenton-like catalyst. *Sci Total Environ* 2017;574:1326-34. DOI PubMed

19. Yang R, Li C, Yuan F, Wu C, Sun Z, Ma R. Synergistic effect of diatomite and Bi self-doping Bi_2MoO_6 on visible light photodegradation of formaldehyde. *Microporous Mesoporous Mater* 2022;339:112003. DOI

20. Sun Z, Li C, Yao G, Zheng S. In situ generated g-C_3N_4/TiO_2 hybrid over diatomite supports for enhanced photodegradation of dye pollutants. *Materials & Design* 2016;94:403-9. DOI

21. Serrà A, Philippe L, Perreault F, Garcia-Segura S. Photocatalytic treatment of natural waters. Reality or hype? *Water Res* 2021;188:116543. DOI PubMed

22. Dheyab MA, Aziz AA, Jameel MS, Noqta OA, Khaniabadi PM, Mehrdel B. Simple rapid stabilization method through citric acid modification for magnetite nanoparticles. *Sci Rep* 2020;10:10793. DOI PubMed PMC

23. Neeli ST, Ramsurn H. Synthesis and formation mechanism of iron nanoparticles in graphitized carbon matrices using biochar from biomass model compounds as a support. *Carbon* 2018;134:480-90. DOI

24. Zhang G, Sun Z, Duan Y, Ma R, Zheng S. Synthesis of nano-TiO_2/diatomite composite and its photocatalytic degradation of gaseous formaldehyde. *Appl Surf Sci* 2017;412:105-12. DOI

25. Marinoni N, Broekmans MA. Microstructure of selected aggregate quartz by XRD, and a critical review of the crystallinity index. *Cem Concr Res* 2013;54:215-25. DOI

26. Liu X, Wang P, Zhai H, et al. Synthesis of synergetic phosphorus and cyano groups (CN) modified g-C_3N_4 for enhanced photocatalytic H_2 production and CO_2 reduction under visible light irradiation. *Appl Catalysis B: Envir* 2018;232:521-30. DOI

27. Khraisheh MA, Al-Ghouti MA, Allen SJ, Ahmad MN. Effect of OH and silanol groups in the removal of dyes from aqueous solution using diatomite. *Water Res* 2005;39:922-32. DOI PubMed

28. Xu L, Gao X, Li Z, Gao C. Removal of fluoride by nature diatomite from high-fluorine water: an appropriate pretreatment for nanofiltration process. *Desalination* 2015;369:97-104. DOI

29. Gerber SJ, Erasmus E. Electronic effects of metal hexacyanoferrates: an XPS and FTIR study. *Mater Chem Phys* 2018;203:73-81. DOI

30. Jia Z, Li T, Zheng Z, et al. The BiOCl/diatomite composites for rapid photocatalytic degradation of ciprofloxacin: Efficiency, toxicity evaluation, mechanisms and pathways. *Chemical Engineering Journal* 2020;380:122422. DOI

31. Antunes VG, Figueroa CA, Alvarez F. Chemisorption competition between H_2O and H_2 for sites on the Si Surface under Xe^+ Ion bombardment: an XPS study. *Langmuir* 2022;38:2109-16. DOI PubMed

32. He H, Luo Z, Yu C. Diatomite-anchored g-C3N4 nanosheets for selective removal of organic dyes. *J Alloys Comp* 2020;816:152652. DOI

33. Shi G, Lv S, Cheng X, Wang X, Li S. Enhanced microwave absorption properties of modified Ni@C nanocapsules with accreted N doped C shell on surface. *J Mater Sci: Mater Electron* 2018;29:17483-92. DOI

34. Gao J, Wang Y, Zhou S, Lin W, Kong Y. A facile one-step synthesis of Fe-doped g-C_3N_4 nanosheets and their improved visible-light photocatalytic performance. *ChemCatChem* 2017;9:1708-15. DOI

35. Chen S, Deng J, Ye C, et al. Degradation of p-arsanilic acid by pre-magnetized Fe0/persulfate system: Kinetics, mechanism, degradation pathways and DBPs formation during subsequent chlorination. *Chem Engin J* 2021;410:128435. DOI

36. Bi L, Gao X, Ma Z, Zhang L, Wang D, Xie T. Enhanced Separation Efficiency of $PtNi_x$/g-C_3N_4 for Photocatalytic Hydrogen Production. *ChemCatChem* 2017;9:3779-85. DOI

37. Garcia-segura S, Tugaoen HO, Hristovski K, Westerhoff P. Photon flux influence on photoelectrochemical water treatment. *Electr Commun* 2018;87:63-5. DOI

38. Li Y, Jin Z, Zhang L, Fan K. Controllable design of Zn-Ni-P on g-C_3N_4 for efficient photocatalytic hydrogen production. *Chinese J Catal* 2019;40:390-402. DOI

39. Xu M, Li J, Yan Y, et al. Catalytic degradation of sulfamethoxazole through peroxymonosulfate activated with expanded graphite loaded $CoFe_2O_4$ particles. *Chem Engin J* 2019;369:403-13. DOI

40. Shao H, Zhao X, Wang Y, et al. Synergetic activation of peroxymonosulfate by Co_3O_4 modified g-C_3N_4 for enhanced degradation of diclofenac sodium under visible light irradiation. *Appl Catal B: Envir* 2017;218:810-8. DOI

41. Chen G, Zhang X, Gao Y, Zhu G, Cheng Q, Cheng X. Novel magnetic MnO2/MnFe2O4 nanocomposite as a heterogeneous catalyst for activation of peroxymonosulfate (PMS) toward oxidation of organic pollutants. *Separ Purif Techn* 2019;213:456-64. DOI

42. Li C, Huang Y, Dong X, et al. Highly efficient activation of peroxymonosulfate by natural negatively-charged kaolinite with abundant hydroxyl groups for the degradation of atrazine. *Appl Catal B: Envir* 2019;247:10-23. DOI

43. An L, Xiao P. Zero-valent iron/activated carbon microelectrolysis to activate peroxydisulfate for efficient degradation of chlortetracycline in aqueous solution. *RSC Adv* 2020;10:19401-9. DOI PubMed PMC

44. Rao Y, Han F, Chen Q, et al. Efficient degradation of diclofenac by LaFeO3-Catalyzed peroxymonosulfate oxidation---kinetics and toxicity assessment. *Chemosphere* 2019;218:299-307. DOI PubMed

45. Zhang X, Duan J, Tan Y, Deng Y, Li C, Sun Z. Insight into peroxymonosulfate assisted photocatalysis over Fe_2O_3 modified TiO_2/diatomite composite for highly efficient removal of ciprofloxacin. *Separ Purif Techn* 2022;293:121123. DOI

46. Kumar S, T S, Kumar B, Baruah A, Shanker V. Synthesis of magnetically separable and recyclable g-C_3N_4-Fe_3O_4 hybrid nanocomposites with enhanced photocatalytic performance under visible-light irradiation. *J Phys Chem C* 2013;117:26135-43. DOI